

Manipulating Picosecond Photoresponse in van der Waals Heterostructure Photodetectors

Zhouxiaosong Zeng, Cuihuan Ge, Kai Braun, Martin Eberle, Yufan Wang, Biyuan Zheng, Chenguang Zhu, Xingxia Sun, Lanyu Huang, Ziyu Luo, Ying Chen, Huigao Duan, Shuangyin Wang, Dong Li, Fei Gao, Anlian Pan,* and Xiao Wang*

Self-powered ultrafast 2D photodetectors have demonstrated great potential in imaging, sensing, and communication. Understanding the intrinsic ultrafast charge carrier generation and separation processes is essential for achieving high-performance devices. However, probing and manipulating the ultrafast photoresponse is limited either by the temporal resolution of the conventional methods or the required sophisticated device configurations. Here, van der Waals heterostructure photodetectors are constructed based on MoS₂/WSe₂ p–n and n–n junctions and manipulate the picosecond photoresponse by combining photovoltaic (PV) and photothermoelectric (PTE) effects. Taking time-resolved photocurrent (TRPC) measurements, a TRPC peak at zero time delay is observed with decay time down to 4 ps in the n–n junction device, in contrast to the TRPC dip in the p–n junction and pure WSe₂ devices, indicating an opposite current polarity between PV and PTE. More importantly, with an ultrafast photocurrent modulation, a transition from a TRPC peak to a TRPC dip is realized, and detailed carrier transport dynamics are analyzed. This study provides a deeper understanding of the ultrafast photocurrent generation mechanism in van der Waals heterostructures and offers a new perspective in instruction for designing more efficient self-powered photodetectors.

photodetection from ultraviolet to the infrared region,^[1–3] the picosecond intrinsic response speed,^[4,5] and the integration of modern silicon technology.^[6–8] The construction of 2D van der Waals heterostructure^[9–12] realizes the high-frequency device applications up to tens of gigahertz,^[13] which provides a potential to outperform the traditional techniques.^[14,15] Moreover, self-powered photodetectors^[16–20] without an external bias are highly desirable in various fields for their low energy consumption and environmental friendliness. Currently, state-of-the-art self-powered photodetectors are mainly based on the pure photovoltaic (PV)^[21–24] or photothermoelectric (PTE)^[18,25] effect, in which photogenerated charge carriers are separated either via a built-in electric field or temperature gradient. Though with conventional electrical transport measurements, such as transfer and output characteristics or photoresponse measurements such as scanning

1. Introduction

Photodetectors based on 2D semiconductors have attracted tremendous research interest because of the broadband

photocurrent microscope (SPCM), the fundamental detection mechanisms of all these self-powered photodetectors have been investigated, the ultrafast time-resolved charge carrier dynamic processes are concealed. Meanwhile, to maximumly utilize the

Z. Zeng, C. Ge, Y. Wang, L. Huang, X. Wang
School of Physics and Electronics
Hunan University
Changsha 410082, China
E-mail: xiao_wang@hnu.edu.cn

K. Braun, M. Eberle
Institute of Physical and Theoretical Chemistry and LISA+
University of Tübingen
Auf der Morgenstelle 18, 72076 Tübingen, Germany
B. Zheng, C. Zhu, X. Sun, Z. Luo, Y. Chen, D. Li, A. Pan
Key Laboratory for Micro-Nano Physics and Technology
of Hunan Province
College of Materials Science and Engineering
Hunan University
Changsha 410082, China
E-mail: anlian.pan@hnu.edu.cn

H. Duan
State Key Laboratory of Advanced Design and Manufacturing for Vehicle
Body College of Mechanical and Vehicle Engineering
Hunan University
Changsha 410082, China

S. Wang
State Key Laboratory of Chem/Bio-Sensing and Chemometrics
College of Chemistry and Chemical Engineering
Hunan University
Changsha 410082, China

F. Gao
Department of Nuclear Engineering and Radiological Sciences
University of Michigan
Ann Arbor, MI 48109, USA

 The ORCID identification number(s) for the author(s) of this article can be found under <https://doi.org/10.1002/adfm.202200973>.

DOI: 10.1002/adfm.202200973

photogenerated carriers and enhance detection performance, combining and manipulating different photodetection mechanisms need further differentiate respective charge carrier dynamics. Hence, understanding the contributions of both PV and PTE effects in one 2D material-based device with an ultrafast method is significant for more efficient high-frequency self-powered photodetector designs beyond state-of-the-art techniques.

Time-resolved photocurrent (TRPC) technique combining pump-probe excitation configuration and photocurrent detection in the micro area has been demonstrated as an effective method for measuring the intrinsic response speed of electric devices. Previous researches have shown that 2D semiconductors, owing to their atomically thin thickness, can exhibit picosecond photocurrent change via PV effect,^[4] PTE effect,^[26] or photoconductive (PC)^[27–29] effect. These photocurrent generation mechanisms individually display a TRPC dip at a small pump-probe delay, where the probe beam induced signal is suppressed because of the saturation in the ground state. With an increase in the delay time, due to the relaxation of excited carriers, a photocurrent recovery with the τ corresponding to the device response time is observed. Despite the extensive TRPC studies focused on the individual photocurrent generation mechanism, direct observation of their interaction and competition remains unexplored, owing to the sophisticated device design and complicated carrier dynamics.

In this work, we demonstrated a comprehensive understanding of the interaction between PV and PTE effects on the picosecond time scale in MoS₂/WSe₂ heterostructure photodetectors. Using a TRPC setup, the ultrafast photoresponse in MoS₂/WSe₂ heterostructures with different WSe₂ thicknesses was investigated. Our results demonstrate an enhanced TRPC signal at zero time delay in MoS₂/1L WSe₂ n–n junctions

with the decay time down to 4 ps, which is distinct from the phenomenon in the MoS₂/25 nm WSe₂ p–n junctions and in other previously reported devices tested by the same technique showing a conventional dip. Pump power-dependent and polarization-dependent photocurrent measurements indicate that this enhanced TRPC signal is derived from the superposition between the PV and PTE currents in opposite directions. Further tuning the electrical field in the heterostructure by the external bias allows us to observe the TRPC transition from a peak to a dip and disentangle the two different dynamic processes.

2. Results and Discussion

2.1. Construction of Heterostructures with Different Carrier Types

TRPC signals could be distinct when a heterostructure photodetector operates at two different current generation mechanisms with different response times (τ_1 , τ_2) (Figure 1a). Under illumination, a PV current from heterostructure is directly generated by the separation of charged photocarriers at the built-in electric field in the depletion region (Figure 1b). While an unbalanced lattice temperature distribution induced by the Seebeck coefficient difference between the two semiconductors creates a photo-thermal voltage, driving a PTE current in the whole device (Figure 1c). With the same or the opposite photocurrent polarity, the resulting TRPC signal from the superposition between PV and PTE current may no longer be a dip at zero time delay. To this end, we design different MoS₂/WSe₂ vertical heterostructure devices with different WSe₂ thicknesses (Figure 1d). We expect a transition from p–n to n–n junctions

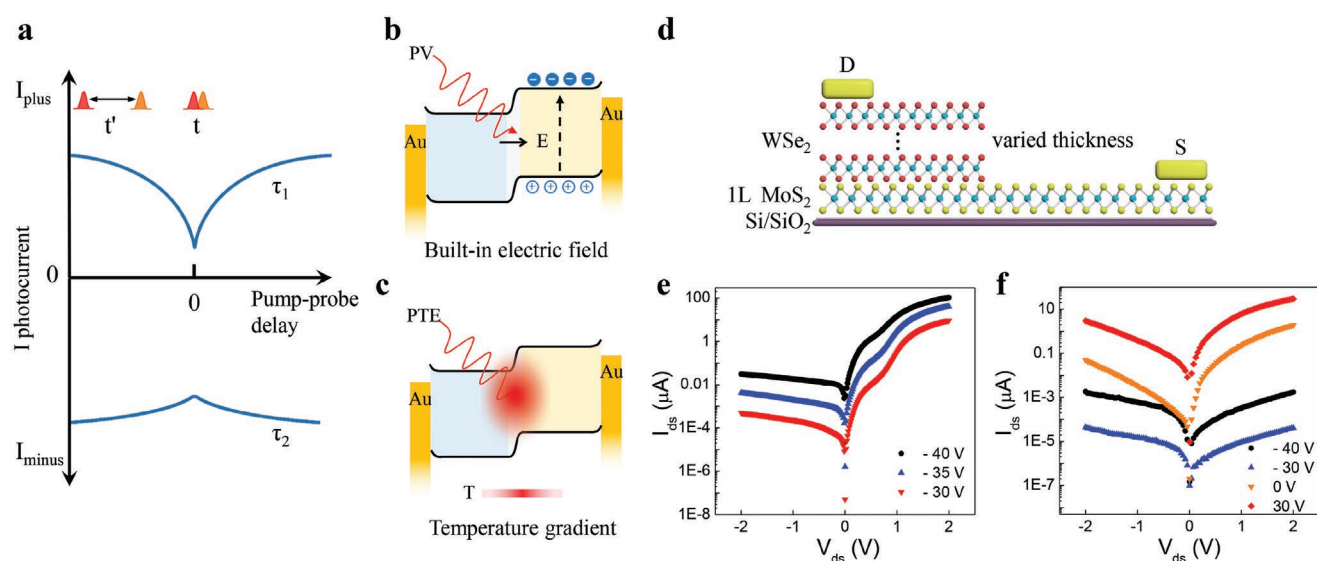


Figure 1. a) Schematic illustration of the simultaneously generated TRPC signal by different photocurrent generation mechanisms. b) Schematic illustration of the PV effect in the heterostructure. c) Schematic illustration of the PTE effect in the heterostructure. d) Schematic illustration of the MoS₂/WSe₂ vertical device with different WSe₂ thicknesses. e) I_{ds} – V_{ds} output characteristic curve in 1L MoS₂/25 nm WSe₂ p–n junction device at different gate voltages, showing the rectification ratio up to 2×10^4 . f) I_{ds} – V_{ds} output characteristic curve in 1L MoS₂/1L WSe₂ n–n junction device at different gate voltages, showing the rectification ratio approximate to 50. V_{ds} refers to the bias on the WSe₂ and a $V_{ds} > 0$ corresponds to a forward bias, while the MoS₂ electrode was grounded.

with the decrease in WSe₂ thickness, because the lattice deformation induced increase of selenium vacancies in thinner WSe₂ can lead to the change in its doping concentration.^[30] Here, two representative devices of MoS₂/25 nm WSe₂ and MoS₂/1L WSe₂ were compared in their electrical transport characteristics. The MoS₂/25 nm WSe₂ device displays a prominent rectifying behavior with a rectification ratio over 10⁴ at negative gate voltages (Figure 1e), which is due to the integration of an ambipolar multilayer WSe₂ on the high electron-doped monolayer MoS₂ (Figure S1a,b, Supporting Information), indicating the formation of a p–n diode. In contrast, with the preferential-n-type monolayer WSe₂ (Figure S1c, Supporting Information), the MoS₂/1L WSe₂ heterostructure exhibits an n–n diode property at various gate voltages with the maximum rectification ratio approximate to 50 (Figure 1f).

2.2. TRPC Dip in MoS₂/WSe₂ p–n Junction

The spatially resolved photocurrent response (see Experimental Section) of the MoS₂/25 nm WSe₂ p–n junction device was characterized by a home-built SPCM at zero source–drain bias under the excitation of a pulsed 780 nm laser. Under 0 V gate voltage, a relatively weak photocurrent appears at the WSe₂ flake (Figure 2b), which is attributed to its larger light absorption and diffusion length compared with monolayer MoS₂. In contrast, the photocurrent maximum was obtained at the MoS₂/WSe₂ junction under the gate voltage of –40 V (Figure 2c), where the photogenerated carriers spontaneously

separate with higher efficiency, indicating that the photocurrent originates from the p–n junction rather than from the Schottky barriers at respective electrodes.^[31,32] Meanwhile, the intensity of this photocurrent in the p–n junction is approximately one order of magnitude larger than the current intensity at 0 V gate voltage under the same excitation power (10 μW), indicating that the photocurrent is mainly derived from the PV effect. We further examined the response time of this vertical p–n junction device by our home-built TRPC setup (see Experimental Section). With the excitation of the pure probe beam, the photocurrent in MoS₂/WSe₂ device exhibits a typical sublinear power dependence (Figure 2d), which can be fitted to the power-law $I_{pc} \approx P^{\alpha}$, where I_{pc} is the generated current intensity and P is the excitation power. With the existence of a pump beam, a suppressed photocurrent at zero time delay with the respect to the pump power further indicates the saturation of the photocurrent. Then the TRPC measurements of the MoS₂/WSe₂ photodetector under typical gate voltages were conducted compared with the pure 25 nm WSe₂ photodetector. All signals display a photocurrent dip at the small pump–probe delay with the different recovery rates. Hence, we extract the response time τ using the equation.

$$\frac{PC(\Delta t)}{PC(\Delta t \rightarrow \infty)} = 1 - A \exp\left(-\frac{\Delta t}{\tau}\right) \quad (1)$$

where the amplitude A and time constant τ are the fitting parameters. The results yield the slowest response speed of 426 ps in pure 25 nm WSe₂ photodetector (black curve in

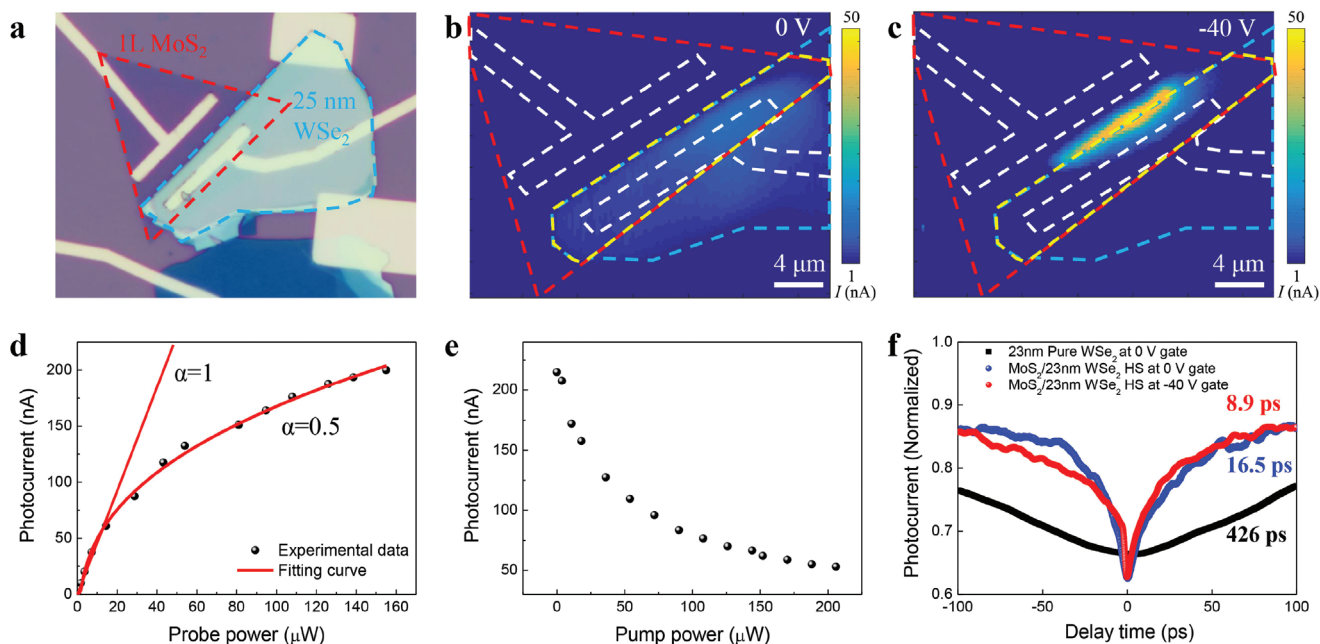


Figure 2. a) Optical image of the 1L MoS₂/25 nm WSe₂ heterostructure photodetector. Dashed lines highlight the CVD grown MoS₂ (red) and exfoliated WSe₂ (blue). b, c) SPCM images obtained at the gate voltages of 0 V and –40 V with an excitation wavelength of 780 nm and $V_{ds} = 0$ V, where the white, red, and blue dashed lines indicate the locations of the electrodes, CVD-grown MoS₂ flake, and exfoliated WSe₂ flake, respectively. The photocurrent is mainly generated at the heterostructure region when the p–n junction is formed. d) Photocurrent as a function of probe power P with no pump. The lines are the power-law fits with $I_{pc} \approx P^1$ and $I_{pc} \approx P^{0.5}$. e) Probe induced photocurrent as a function of pump power at 0 ps delay time. f) Time-resolved photocurrent measurements in pure 25 nm WSe₂ at $V_g = 0$ V (black), MoS₂/25 nm WSe₂ heterostructure at $V_g = 0$ V (blue), and at $V_g = -40$ V (red), where ≈ 50 times faster response is obtained in p–n junction compared to the pure material.

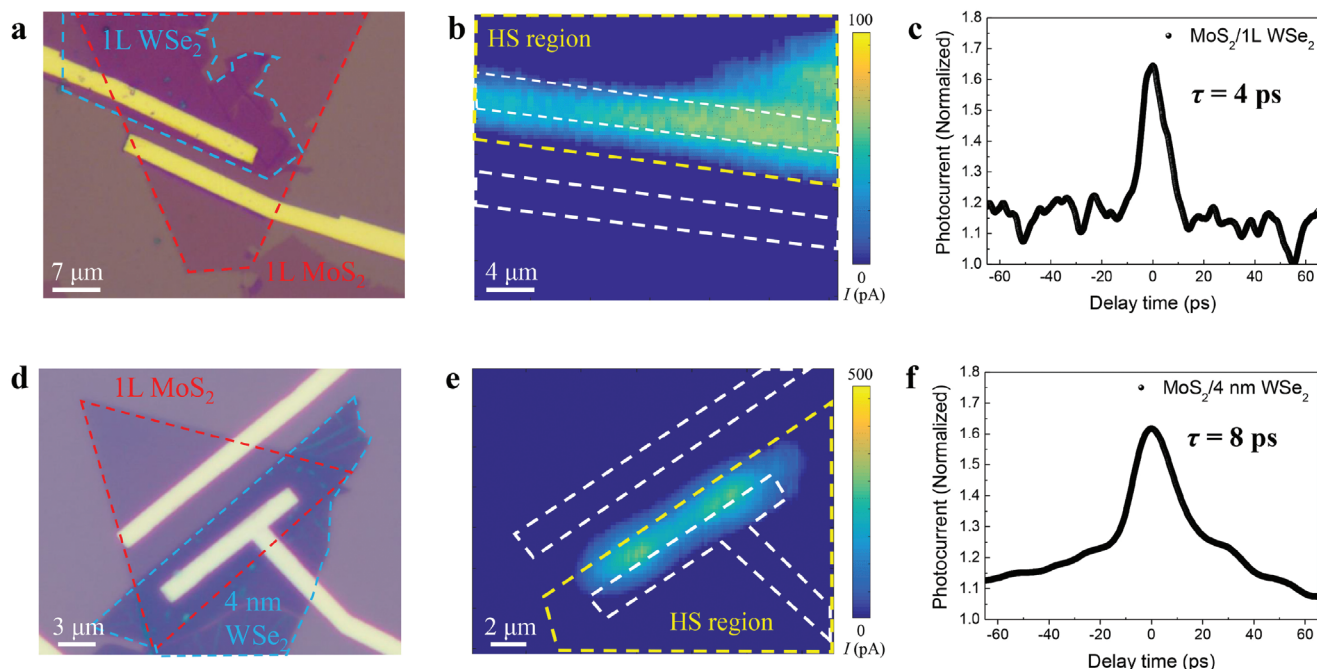


Figure 3. a,d) Optical images of the MoS₂/1L WSe₂ heterostructure photodetector and MoS₂/4 nm WSe₂ heterostructure photodetector. b,e) Corresponding SPCM images obtained with the excitation wavelength of 780 nm on the devices in (a) and (d) with the $V_{ds} = 0$ V and $V_g = 0$ V, where the white and yellow dashed lines indicate the locations of the electrodes and heterostructure region, respectively. The obtained photocurrent gets closer to the electrode with the decrease of WSe₂ thickness. c,f) TRPC measurements corresponding to the devices in (a) and (d), where ultrafast positive signals are obtained at zero delay time.

Figure 2f), while approximate 25-fold and 50-fold enhancements were observed in heterostructure under 0 V (blue curve in Figure 2f) and -40 V (red curve in Figure 2f) gate voltages, which is attributed to the more effective carrier separation and extraction by the type-II heterostructure^[33,34] and p–n junction.^[31,35] Thus far, the significant role of the PV effect in the p–n junction is apparent, while the participation of the PTE effect is hard to extract because of its same polarity and a relatively small contribution to the PV current.

2.3. TRPC Peak in MoS₂/WSe₂ n–n Junction

Considering the polarity of the PTE current could be influenced by the carrier type^[36–38] in heterostructures, we further investigated the MoS₂/1L WSe₂ n–n junction photodetectors. In SPCM measurements, compared with the p–n junction device, the photocurrent map demonstrates a similar photocurrent maximum appearing at the n–n junction, but with the decrease in WSe₂ thickness, the generated photocurrent was approaching the electrode (Figure 3b). This phenomenon could be an indication that the PTE effect contributed more photocurrent, and therefore we performed the TRPC studies. An obviously enhanced peak signal at zero pump–probe time delay was observed with a response time approximate to 4 ps (Figure 3c), which is distinct from the previously reported phenomenon in transition metal dichalcogenides (TMDCs)^[4,28] and their heterostructures^[27,29,39–41] by the same measurement technique. Meanwhile, the above phenomenon can be observed in another MoS₂/4 nm WSe₂ n–n junction device (Figure 3d–f) with a little

slowed response time to 8 ps, which can be explained as the increased out-of-plane drift time in thicker devices according to the transit time expression of $\tau_{\text{tran}} = L^2/\mu V_{\text{bias}}$.^[41]

To elucidate these unique signals, we further performed pump power and polarization-dependent photocurrent measurements. In TRPC experiments, with the increase in pump power, an enhanced photocurrent signal at zero time delay gradually appeared (Figure 4a), while the photocurrent background was suppressed. We extracted the photocurrent changes at the background and at the peak in absolute value, where a linearly increased photocurrent enhancement at zero time delay and a linearly decreased photocurrent background with the increase in pump power were shown (Figure 4b). Besides, photocurrent polarization could distinguish different photocurrent generation mechanisms because of different plasmonic hot carrier injection efficiencies from a metal electrode to a semiconductor.^[42] Here, the enhanced photocurrent peak in MoS₂/1L WSe₂ n–n junction was anisotropic and had an anisotropy ratio of 1.63 (Figure S7e, Supporting Information), which was between the anisotropy ratios of 1.1 in PV response and 4.25 in PTE response in our study on the pure MoS₂ (Figure S7b,c, Supporting Information). While no clear plasmonic effect induced photocurrent enhancement similar to the previous works^[43,44] was observed, possibly because the input electric field is difficult to be confined with the channel width of 5 to 7 μm in our case. The results in power-dependent and polarization-dependent TRPC both indicate that the TRPC peak could arise from the combined photocurrent in both PV and PTE effects. Considering the generated photocurrent can be easily modulated by the external bias for a relatively weak built-in electric field in an n–n junction, we further conducted TRPC

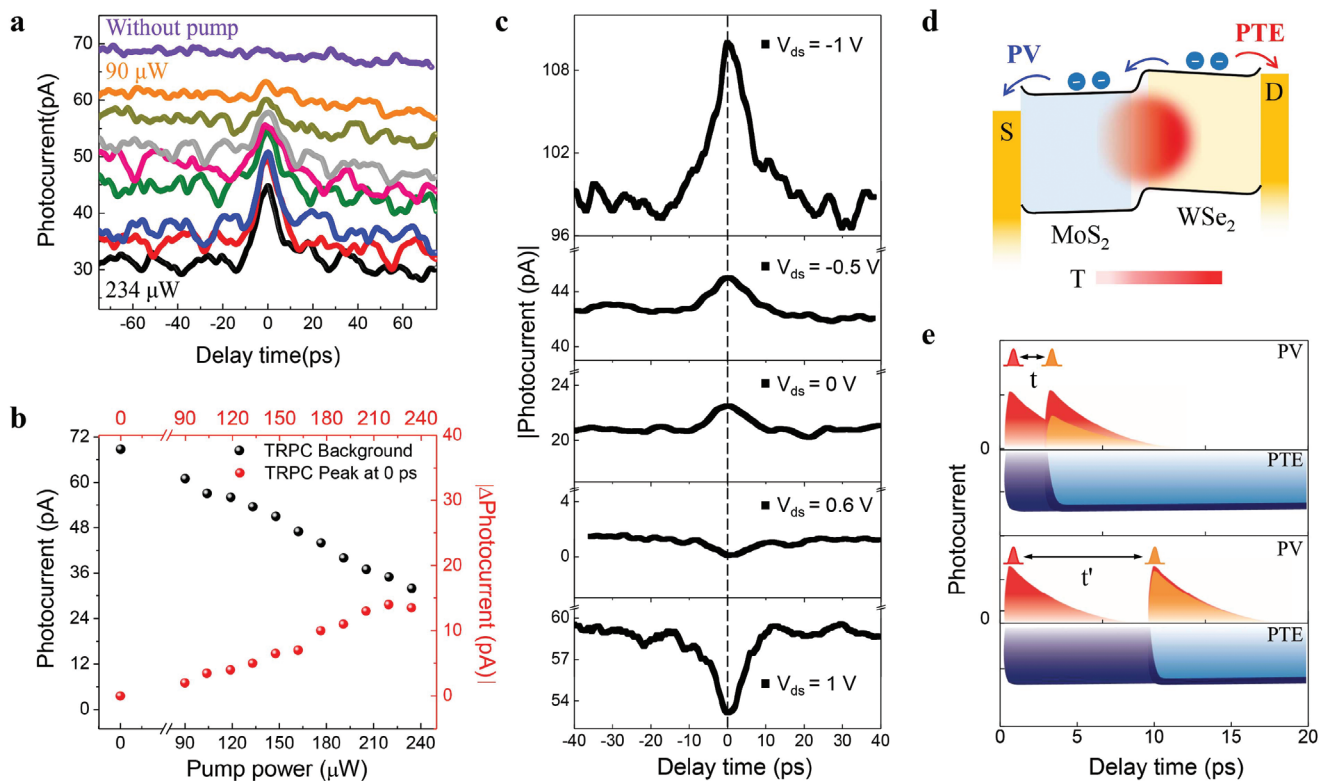


Figure 4. a) TRPC measurements at different pump powers. b) Extracted background photocurrent (black) and the $|\Delta PC|$ (red) change with the increase of pump power. The background photocurrent is defined as the photocurrent with the pump–probe delay $t \rightarrow \infty$, while the $|\Delta PC|$ is defined as the difference between the photocurrent ($t = 0$) and photocurrent ($t \rightarrow \infty$). c) TRPC measurements with different V_{ds} biases applied at the WSe₂ electrode. When the V_{ds} is reverse biased, an enhanced signal is obtained at the 0 ps time delay. When the V_{ds} is forward biased, a suppressed signal is obtained at the 0 ps time delay. d) Schematic illustration of the opposite PV and PTE current generation in one device after pulsed laser illumination, where the blue arrows indicate the generation of negative PV current by the built-in electric field while the red arrow indicates the WSe₂ dominant positive PTE current due to its larger Seebeck coefficient. e) Schematic illustration of the photocurrent superposition between PV and PTE effect in MoS₂/WSe₂ n–n junction photodetector. Here the PV (PTE) current in the red (dark blue) area is induced by the individual pump or probe excitation, while the PV (PTE) current in the orange (light blue) area is induced by the probe excitation with the pump.

measurements with different drain voltages. When applied bias was in the same direction as the built-in electric field ($V_{ds} < 0$ V), an increased TRPC signal and an almost unchanged peak proportion were found with the increase in drain voltages, demonstrating only the photocurrent intensity has changed. Whereas varying the junction from reverse bias to forward bias ($V_{ds} > 0$ V), a TRPC signal transition from a peak to a dip at zero time delay was observed at $V_{ds} = 0.6$ V (Figure 4c), and this phenomenon appeared more prominent with larger bias.

2.4. Analysis of PV and PTE Effects

As the TRPC signal can be modulated from the distinct peak to the normal dip under the external bias, we consider that the PV and PTE effects contribute to a photocurrent with opposite polarities in the MoS₂/WSe₂ n–n junction at the $V_{ds} = 0$. Under the 780 nm laser excitation, the absorption of the WSe₂ layer generates electron–hole pairs, which are separated by the built-in electrical field at the junction, contributing to the negative PV current (blue arrow process in Figure 4d). Meanwhile, local heating created by the laser illumination is converted into a voltage difference across the junction, which produces a PTE current. In a

traditional metal–semiconductor–metal (MSM) structure, taking n-type materials as an example, the illumination near the contact leads to the electron concentration increase and a tilt of energy band, where excessive electrons diffuse to another cold contact contributing to a PTE current with the same polarity of PV current.^[45,46] Whereas in our case, the temperature increase at the MoS₂/WSe₂ junction induces a competition of the PTE current flow by these two materials depending on the Seebeck coefficient difference between them. Previous reports demonstrate that the monolayer TMDCs exhibit similar thermoelectric properties with a comparable intrinsic Seebeck coefficient.^[47,48] However, thermopower can be influenced by the charge carrier density, and the Seebeck coefficient will monotonously increase with the decrease in carrier doping concentration,^[46,49] according to the Mott formula. Hence compared with highly doped MoS₂, the lowly doped WSe₂ has a larger Seebeck coefficient, and the diffusion of its electrons to the drain contact dominates the polarity of PTE current (red arrow process in Figure 4d), contributing an opposite effect to the PV current. In this situation, the temperature difference induced voltage also reduces the barrier between MoS₂ and WSe₂, making the generation of PTE current easier.

On the temporal scale, the PV effect in our MoS₂/WSe₂ n–n junction leads to a response time of several picoseconds because

of the short carrier lifetime in thin-layered TMDCs^[4,50] and their heterostructures.^[27] While an almost unchanged TRPC was obtained by the pure PTE effect in the 1L MoS₂ device (Figure S9c, Supporting Information), which is attributed to the longstanding cooling time of the excited hot carriers through the slow coupling to acoustic phonons. Hence, we propose that with the pure probe excitation, the PV (red area in Figure 4e) and PET (dark blue area in Figure 4e) current first has an opposite polarity, and with the existence of a pump beam, an incompletely offset photocurrent by the opposite PV and PTE effects is achieved in small pump–probe delay (the superposition of orange and light blue area in Figure 4e upper plane), contributing a relatively large net photocurrent. With the increase in delay time, the suppressed PV current quickly recovered, while the PTE current stayed invariant for a longer hot carrier relaxation time. Therefore, the recovered PV current induces a larger photocurrent offset, and the whole photocurrent is reduced at the large pump–probe delay (the superposition of orange and light blue area in Figure 4e lower plane).

3. Conclusion

In summary, using TRPC measurements in combination with SPCM, we provided a comprehensive picture of the tangled PTE effect with the PV effect in the generation of photocurrent on the picosecond time scale. The carrier type change in MoS₂/WSe₂ junction photodetector with different WSe₂ thicknesses determined the PV and PTE current polarity. An enhanced TRPC signal at zero pump–probe delay in MoS₂/1L WSe₂ n–n junction in contrast to the dip in MoS₂/25 nm WSe₂ p–n junction reflected an opposite polarity of PV and PTE current, which can be further modulated by the external bias. A deeper understanding of PV and PTE mechanisms in van der Waals heterostructures can be an instruction for designing more efficient photodetectors.

4. Experimental Section

Sample Preparation and Device Fabrication: MoS₂/WSe₂ vertical heterostructure devices with different thicknesses were fabricated via transferring mechanically exfoliated WSe₂ onto the CVD synthesized monolayer MoS₂. In preparation of MoS₂ samples, the powders of sulfur and MoO₃ in two ceramic boats were placed on the upstream side and the center of the furnace, respectively. A cleaned silicon substrate with a 300-nm-thick silicon dioxide layer was face-down mounted on the MoO₃ boat. The furnace temperature was ramped up to 780 °C and kept at that temperature for 10 min with an Ar gas flow rate of 150 standard cubic centimeter per minute (sccm). After that, the furnace was cooled to room temperature naturally. Then a WSe₂ flake mechanically exfoliated onto transparent polydimethylsiloxane (PDMS) was aligned and transferred onto the synthesized MoS₂ flake with the help of a microscope. Cr/Au (10/50 nm) conducting electrodes on top of MoS₂/WSe₂ heterostructures with a channel length of 5 to 7 μm were fabricated using standard electron beam lithography (EBL), metal thermal evaporation, and lift-off processes.

Basic Characterization: Atomic force microscopy (AFM) (Bruker Dimension Icon) in the tapping mode was used to identify the thickness of the samples. Raman, photoluminescence, and time-resolved photoluminescence (TRPL) measurements of the samples were taken using a confocal microscope (WITec, alpha-300) equipped with a 50×

objective lens (Zeiss EC Epiplan). The excitation source of the Raman and PL spectra was a 532 nm continuous-wave laser, and the laser beam was focused to 1 μm on the samples. The TRPL measurements of the samples were detected with a streak camera system (Hamamatsu, C10910) using laser pulses at 400 nm (repetition rate of 80 MHz, pulse width of 100 fs) as the excitation source. The electrical properties were measured with an Agilent-B1500 semiconductor analyzer in a LakeShore vacuum chamber of 10⁻⁴ Pa.

SPCM and TRPC Measurements: SPCM and TRPC were performed on the home-built setup. In SPCM measurements, a 780 nm fiber laser (NPI Rainbow 780 OEM) with a pulse width of 80 fs and a 488 nm continuous-wave laser was chopped by a mechanical chopper at 1050 Hz and then focused onto the sample by a long working distance objective (Olympus LMPLFLN 50×) near the diffraction limit. The generated photocurrent was collected by a lock-in amplifier (Stanford SR830) at the chopped frequency with a background noise of ≈0.2 pA. The SPCM measurements with a resolution close to the diffraction limit were performed by raster scanning the entire device mounted on a piezoelectric translation stage (Piezoconcept LT3) according to the fixed laser spot. In TRPC studies, a 780 nm pulse laser was split into two independent beams to form a pump–probe measurement configuration, and the probe beam was chopped so that the lock-in amplifier could only measure its photocurrent. The pump beam was delayed by different path lengths, with the delay time precisely controlled by a mechanical delay stage (Thorlabs DDSM100/M). The pump and probe beams were recombined by a beam splitter after the delay line stage and focused onto the sample using the same long working distance objective. The temporal resolution of the TRPC set-up was about 1 ps. A gate voltage was applied by a Source Measure Unit (Keithley 2400) in gate-dependent SPCM and TRPC measurements.

Supporting Information

Supporting Information is available from the Wiley Online Library or from the author.

Acknowledgements

Z.Z. and C.G. contributed equally to this work. This work was supported by the National Natural Science Foundation of China (Nos. 52022029, 91850116, 51772084, U19A2090), the Sino-German Center for Research Promotion (No. GZ1390), and the Hunan Provincial Natural Science Foundation of China (Nos. 2018RS3051, 2019XK2001).

Conflict of Interest

The authors declare no conflict of interest.

Data Availability Statement

The data that support the findings of this study are available from the corresponding author upon reasonable request.

Keywords

2D materials, photodetectors, scanning photocurrent mapping, time-resolved photocurrent, van der Waals heterostructures

Received: January 24, 2022

Revised: March 2, 2022

Published online: May 6, 2022

- [1] Q. X. Qiu, Z. M. Huang, *Adv. Mater.* **2021**, *33*, 2008126.
- [2] F. N. Xia, H. Wang, D. Xiao, M. Dubey, A. Ramasubramaniam, *Nat. Photonics* **2014**, *8*, 899.
- [3] C. Y. Liu, J. S. Guo, L. W. Yu, J. Li, M. Zhang, H. Li, Y. C. Shi, D. X. Dai, *Light Sci. Appl.* **2021**, *10*, 123.
- [4] H. N. Wang, C. J. Zhang, W. M. Chan, S. Tiwari, F. Rana, *Nat. Commun.* **2015**, *6*, 8831.
- [5] P. Ma, Y. Salamin, B. Baeuerle, A. Josten, W. Heni, A. Emboras, J. Leuthold, *ACS Photonics* **2019**, *6*, 154.
- [6] F. H. L. Koppens, T. Mueller, P. Avouris, A. C. Ferrari, M. S. Vitiello, M. Polini, *Nat. Nanotechnol.* **2014**, *9*, 780.
- [7] D. Akinwande, C. Huyghebaert, C. H. Wang, M. I. Serna, S. Goossens, L. J. Li, H. S. P. Wong, F. H. L. Koppens, *Nature* **2019**, *573*, 507.
- [8] K. C. Zhu, C. Wen, A. A. Aljarb, F. Xue, X. M. Xu, V. Tung, X. X. Zhang, H. N. Alshareef, M. Lanza, *Nat. Electron.* **2021**, *4*, 775.
- [9] X. Zhou, X. Z. Hu, S. S. Zhou, H. Y. Song, Q. Zhang, L. J. Pi, L. Li, H. Q. Li, J. T. Lu, T. Y. Zhai, *Adv. Mater.* **2018**, *30*, 1703286.
- [10] F. K. Wang, P. Luo, Y. Zhang, Y. Huang, Q. F. Zhang, Y. Li, T. Y. Zhai, *Sci. China Mater.* **2020**, *63*, 1537.
- [11] F. K. Wang, J. Wu, Y. Zhang, S. J. Yang, N. Zhang, H. Q. Li, T. Y. Zhai, *Sci. China Mater.* **2022**, *65*, 451.
- [12] L. X. Liu, T. Y. Zhai, *Infomat* **2021**, *3*, 3.
- [13] N. Flory, P. Ma, Y. Salamin, A. Emboras, T. Taniguchi, K. Watanabe, J. Leuthold, L. Novotny, *Nat. Nanotechnol.* **2020**, *15*, 118.
- [14] A. Rogalski, *Prog. Quantum Electron.* **2003**, *27*, 59.
- [15] A. Rogalski, *Prog. Quantum Electron.* **2012**, *36*, 342.
- [16] M. Buscema, J. O. Island, D. J. Groenendijk, S. I. Blanter, G. A. Steele, H. S. J. van der Zant, A. Castellanos-Gomez, *Chem. Soc. Rev.* **2015**, *44*, 3691.
- [17] M. S. Long, P. Wang, H. H. Fang, W. D. Hu, *Adv. Funct. Mater.* **2019**, *29*, 1803807.
- [18] X. W. Lu, L. Sun, P. Jiang, X. H. Bao, *Adv. Mater.* **2019**, *31*, 1902044.
- [19] J. Fang, Z. Zhou, M. Xiao, Z. Lou, Z. Wei, G. Shen, *Infomat* **2020**, *2*, 291.
- [20] M. Wu, Y. Xiao, Y. Zeng, Y. Zhou, X. Zeng, L. Zhang, W. Liao, *Infomat* **2021**, *3*, 362.
- [21] F. Wu, Q. Li, P. Wang, H. Xia, Z. Wang, Y. Wang, M. Luo, L. Chen, F. S. Chen, J. S. Miao, X. S. Chen, W. Lu, C. X. Shan, A. L. Pan, X. Wu, W. C. Ren, D. Jariwala, W. D. Hu, *Nat. Commun.* **2019**, *10*, 4663.
- [22] C. J. Zhou, S. Y. Zhang, Z. Lv, Z. C. Ma, C. Yu, Z. H. Feng, M. S. Chan, *NPJ 2D Mater. Appl.* **2020**, *4*, 46.
- [23] X. K. Zhang, B. S. Liu, L. Gao, H. H. Yu, X. Z. Liu, J. L. Du, J. K. Xiao, Y. H. Liu, L. Gu, Q. L. Liao, Z. Kang, Z. Zhang, Y. Zhang, *Nat. Commun.* **2021**, *12*, 1522.
- [24] S. Ghosh, A. Varghese, K. Thakar, S. Dhara, S. Lodha, *Nat. Commun.* **2021**, *12*, 3336.
- [25] J. Liu, F. N. Xia, D. Xiao, F. J. G. de Abajo, D. Sun, *Nat. Mater.* **2020**, *19*, 830.
- [26] D. Sun, G. Aivazian, A. M. Jones, J. S. Ross, W. Yao, D. Cobden, X. D. Xu, *Nat. Nanotechnol.* **2012**, *7*, 114.
- [27] M. Massicotte, P. Schmidt, F. Violla, K. G. Schadler, A. Reserbat-Plantey, K. Watanabe, T. Taniguchi, K. J. Tielrooij, F. H. L. Koppens, *Nat. Nanotechnol.* **2016**, *11*, 42.
- [28] K. T. Vogt, S. F. Shi, F. Wang, M. W. Graham, *J. Phys. Chem. C* **2020**, *124*, 15195.
- [29] M. Massicotte, P. Schmidt, F. Violla, K. Watanabe, T. Taniguchi, K. J. Tielrooij, F. H. L. Koppens, *Nat. Commun.* **2016**, *7*, 12174.
- [30] Z. Wang, H. Xia, P. Wang, X. H. Zhou, C. S. Liu, Q. H. Zhang, F. Wang, M. L. Huang, S. Y. Chen, P. S. Wu, Y. F. Chen, J. F. Ye, S. Y. Huang, H. G. Yan, L. Gu, J. S. Miao, T. X. Li, X. S. Chen, W. Lu, P. Zhou, W. D. Hu, *Adv. Mater.* **2021**, *33*, 2104942.
- [31] R. Cheng, D. H. Li, H. L. Zhou, C. Wang, A. X. Yin, S. Jiang, Y. Liu, Y. Chen, Y. Huang, X. F. Duan, *Nano Lett.* **2014**, *14*, 5590.
- [32] C. H. Lee, G. H. Lee, A. M. van der Zande, W. C. Chen, Y. L. Li, M. Y. Han, X. Cui, G. Arefe, C. Nuckolls, T. F. Heinz, J. Guo, J. Hone, P. Kim, *Nat. Nanotechnol.* **2014**, *9*, 676.
- [33] H. M. Zhu, J. Wang, Z. Z. Gong, Y. D. Kim, J. Hone, X. Y. Zhu, *Nano Lett.* **2017**, *17*, 3591.
- [34] F. Li, B. Y. Xu, W. Yang, Z. Y. Qi, C. Ma, Y. J. Wang, X. H. Zhang, Z. R. Luo, D. L. Liang, D. Li, Z. W. Li, A. L. Pan, *Nano Res.* **2020**, *13*, 1053.
- [35] Y. Chen, X. D. Wang, L. Huang, X. T. Wang, W. Jiang, Z. Wang, P. Wang, B. M. Wu, T. Lin, H. Shen, Z. M. Wei, W. D. Hu, X. J. Meng, J. H. Chu, J. L. Wang, *Nat. Commun.* **2021**, *12*, 4030.
- [36] N. M. Gabor, J. C. W. Song, Q. Ma, N. L. Nair, T. Taychatanapat, K. Watanabe, T. Taniguchi, L. S. Levitov, P. Jarillo-Herrero, *Science* **2011**, *334*, 648.
- [37] J. C. W. Song, M. S. Rudner, C. M. Marcus, L. S. Levitov, *Nano Lett.* **2011**, *11*, 4688.
- [38] J. Zhang, H. J. Liu, L. Cheng, J. Wei, J. H. Liang, D. D. Fan, P. H. Jiang, L. Sun, J. Shi, *J. Mater. Chem. C* **2016**, *4*, 991.
- [39] M. Massicotte, F. Violla, P. Schmidt, M. B. Lundeberg, S. Latini, S. Haastrop, M. Danovich, D. Davydovskaya, K. Watanabe, T. Taniguchi, V. I. Fal'ko, K. S. Thygesen, T. G. Pedersen, F. H. L. Koppens, *Nat. Commun.* **2018**, *9*, 1633.
- [40] Y. C. Kim, V. T. Nguyen, S. Lee, J. Y. Park, Y. H. Ahn, *ACS Appl. Mater. Interfaces* **2018**, *10*, 5771.
- [41] Z. Zeng, K. Braun, C. Ge, M. Eberle, C. Zhu, X. Sun, X. Yang, J. Yi, D. Liang, Y. Wang, L. Huang, Z. Luo, D. Li, A. Pan, X. Wang, *Fundam. Res.* **2021**, *9*.
- [42] T. Hong, B. Chamlagain, S. R. Hu, S. M. Weiss, Z. X. Zhou, Y. Q. Xu, *ACS Nano* **2015**, *9*, 5357.
- [43] J. R. Fang, D. Wang, C. T. DeVault, T. F. Chung, Y. P. Chen, A. Boltasseva, V. M. Shalae, A. V. Kildishev, *Nano Lett.* **2017**, *17*, 57.
- [44] Y. L. Guo, L. W. Guo, K. Y. Zhou, J. W. Yang, Z. Xu, X. D. Bai, *AIP Adv.* **2021**, *11*, 085124.
- [45] M. Buscema, M. Barkelid, V. Zwiller, H. S. J. van der Zant, G. A. Steele, A. Castellanos-Gomez, *Nano Lett.* **2013**, *13*, 358.
- [46] C. C. Wu, D. Jariwala, V. K. Sangwan, T. J. Marks, M. C. Hersam, L. J. Lauhon, *J. Phys. Chem. Lett.* **2013**, *4*, 2508.
- [47] D. L. Li, Y. N. Gong, Y. X. Chen, J. M. Lin, Q. Khan, Y. P. Zhang, Y. Li, H. Zhang, H. P. Xie, *Nano-Micro Lett.* **2020**, *12*, 36.
- [48] D. Wickramaratne, F. Zahid, R. K. Lake, *J. Chem. Phys.* **2014**, *140*, 124710.
- [49] J. Wu, H. Schmidt, K. K. Amara, X. F. Xu, G. Eda, B. Ozyilmaz, *Nano Lett.* **2014**, *14*, 2730.
- [50] H. N. Wang, C. J. Zhang, F. Rana, *Nano Lett.* **2015**, *15*, 8204.